Electronic Supporting Information (ESI) for

Silver-Inserted Zinc Rhodium Oxide and Bismuth Vanadium Oxide Heterojunction Photocatalyst for Overall Pure-Water Splitting under Red Light

Ryoya Kobayashi,[a] Kazuki Kurihara,[b] Toshihiro Takashima,[c] Bunsho Ohtani,[d] and Hiroshi Irie*[c]

[a] Special Doctoral Program for Green Energy Conversion Science and Technology, Interdisciplinary Graduate School of Medicine and Engineering, University of Yamanashi, 4-3-11 Takeda, Kofu, Yamanashi 400-8511, Japan
[b] Department of Applied Chemistry, Interdisciplinary Graduate School of Medicine and Engineering, University of Yamanashi, 4-3-11 Takeda, Kofu, Yamanashi 400-8511, Japan
[c] Clean Energy Research Center, University of Yamanashi, 4-3-11 Takeda, Kofu, Yamanashi 400-8511, Japan
[d] Catalysis Research Center, Hokkaido University, Nishi 10, Kita 21, Sapporo 001-0021, Japan

Contents

ESI. 1 Transmission spectra of $AgNO_3$ solution (0.1 mol/L) and $Ce(SO_4)_2$ solution (0.1 mol/L) (Fig. S1)

$AgNO_3$ solution is usually utilized when Ag^+ is applied as the sacrificial agent because it is transparent to irradiated light with a wavelength above ~350 nm as shown in Fig. S1. In the present study, we utilized $Ce(SO_4)_2$ solution, which was yellowish and transparent, and it can be seen from Fig. S1 that the solution absorbs visible light up to a wavelength of ~550 nm. The $Ce(SO_4)_2$ solution has no absorption at the wavelengths of 610 and 700 nm of the used light for irradiation. Thus, the $Ce(SO_4)_2$ solution was an appropriate source of Ce^{4+} for the sacrificial agent in the present study.

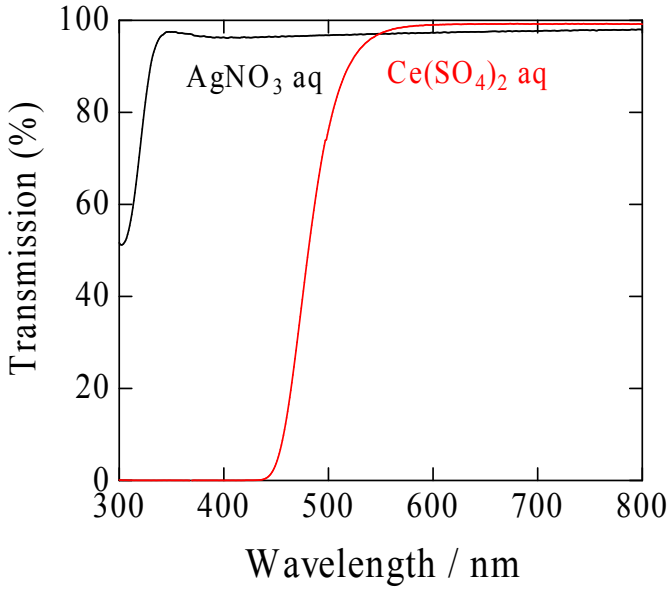

Fig. S1 Transmission spectra of $AgNO_3$ solution (0.1 mol/L) and $Ce(SO_4)_2$ solution (0.1 mol/L).

ESI. 2 XPS analyses of $ZnRh_2O_4/Ag/Bi_4V_2O_{11}$ photocatalyst (Figs. S2, S3).

XRD peaks originated from Ag could not be detected, so we measured the Ag 3d XPS to confirm the existence and valency of Ag as shown in Fig. S2. In Fig. S2, the Ag 3d spectra of Ag and Ag_2O were also included. First, the spectrum of Ag was detected from the $ZnRh_2O_4/Ag/Bi_4V_2O_{11}$ photocatalyst, indicating the existence of Ag species. In addition, the valency of Ag in the photocatalyst was proved to be mainly zero (Ag^0) and partially 1+ (Ag^+, Ag_2O). The oxidized state (Ag^+) is plausible because Ag was surrounded by oxides, $ZnRh_2O_4$ and $Bi_4V_2O_{11}$. In addition, the observation of the partially Ag^+ might be the evidence that Ag is connected to $ZnRh_2O_4$ and $Bi_4V_2O_{11}$. So, we concluded that the Ag was inserted as the metallic one between $ZnRh_2O_4$ and $Bi_4V_2O_{11}$ by combining the STEM/EDS results in ESI. 3 and 4 later.

We evaluated the Ag content by XPS as shown in Figs. S3a-S3e, taking peak areas of Ag 3d, Zn 2p, Rh 3d, Bi 4f, and V 2s and their atomic sensitivity factors into considerations. As shown in Fig. S3e, the peak of V 2s was partially overlapped by that of Rh 3s, so the peak separation was employed and the peak area of V 2s was obtained. Then, Ag was included ~3 atomic percent. The ratio of Zn/Rh was 0.554, slightly deviated from the stoichiometric ratio of 0.5, however, that of Bi/V was 1.65, indicating that Bi vacancy was generated. We have already reported the Ag vacancy was produced after the HNO_3 treatment of $ZnRh_2O_4/Ag/AgSbO_3$, and $ZnRh_2O_4/Ag/Ag_{1-x}SbO_{3-y}$ was formed. Similar phenomenon was proceeded in the present photocatalyst. It should be noted that the amount of generated Ag vacancy was so large that the XRD peaks of $Ag_{1-x}SbO_{3-y}$ shifted to the lower angle compared to the non-treated $AgSbO_3$. In the present study, the XRD peak shifts were not observed before and after the HNO_3 treatment of $Bi_4V_2O_{11}$, so we depict the HNO_3-treated $Bi_4V_2O_{11}$ as simply $Bi_4V_2O_{11}$.

We have successfully removed Ag without forming deficiencies by the treatment with ammonia solution instead of HNO_3. The results will be reported elsewhere.

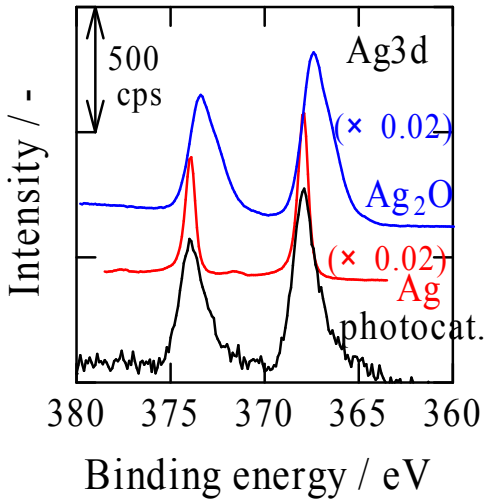

Fig. S2 Ag 3d XPS spectra of $ZnRh_2O_4/Ag/Bi_4V_2O_{11}$ photocatalyst (denoted as photocat.), commercially available Ag_2O and Ag. Those spectra were drawn after calibration with the C 1s peak, derived from a surface-contaminant hydrocarbon that had a binding energy of 284.5 eV.

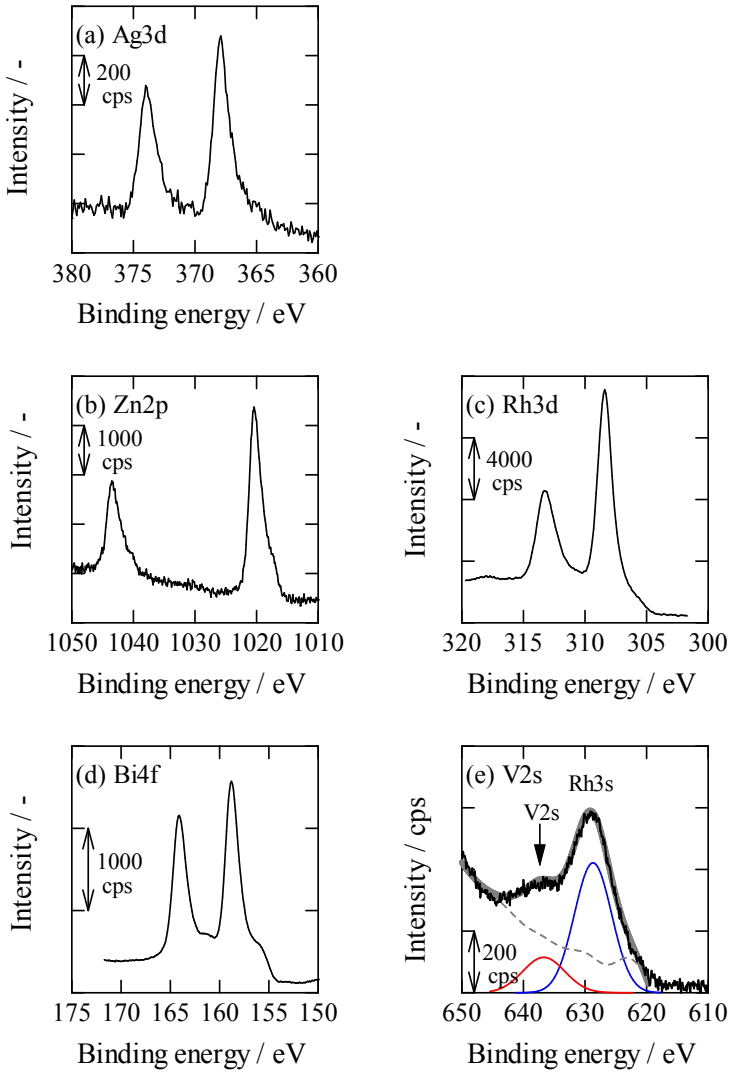

Fig. S3 XPS spectra of $ZnRh_2O_4/Ag/Bi_4V_2O_{11}$, (a) Ag 4d, (b) Zn 2p, (c)Rh 3d, (d) Bi4f, and (e) V2s. In (e), experimental XPS spectrum (black line), fitted curve (gray bold line), background curve (gray broken line), and component peaks of V 2s (red line) and Rh 3s (blue line) determined by deconvolution of the experimental XPS spectrum data. All spectra were calibrated with the C 1s peak, derived from a surface-contaminant hydrocarbon that had a binding energy of 284.5 eV.

ESI. 3 STEM $ZnRh_2O_4/Ag/Bi_4V_2O_{11}$ photocatalyst (Fig. S4).

STEM images (Figs. S4a and S4b) and EDS element maps (Figs. S4d−S4h) of Ag, Bi, Rh, V, and Zn, respectively, are shown for $ZnRh_2O_4/Ag/Bi_4V_2O_{11}$ after HNO_3 treatment (Fig. S4a is the same as Fig. 4a, but is rotated). Fig. S4c is the overlapped color image of Figs. S4d-S4h. Fig. S4b is the enlargement of Fig. S4a. As clearly seen in Fig. S4c, Ag particles are connected with both $ZnRh_2O_4$ and $Bi_4V_2O_{11}$ particles.

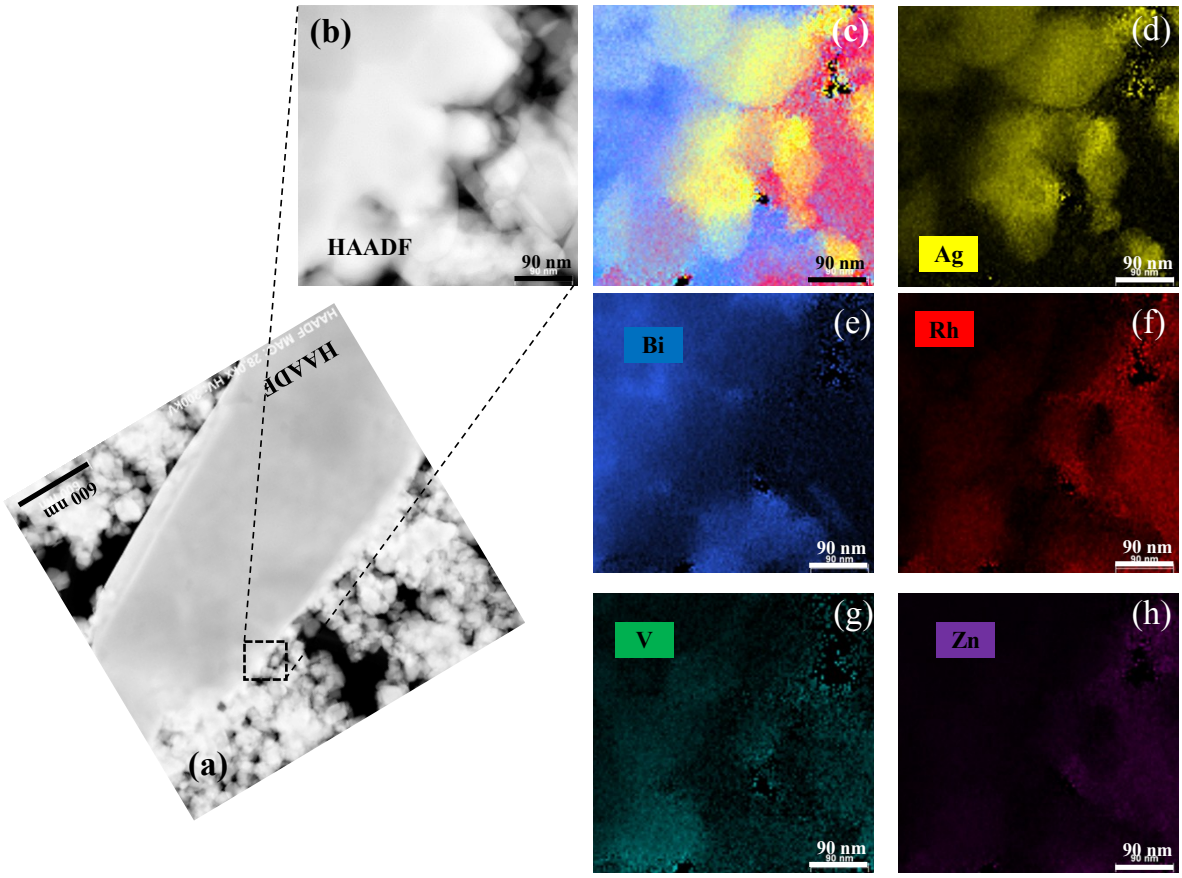

Fig. S4 STEM images (a and b) and EDS element maps (c−h) in which yellow (d), blue (e), red (f), blue-green (g), and purple (h) colors correspond to Ag, Bi, Rh, V, and Zn, respectively, for $ZnRh_2O_4/Ag/Bi_4V_2O_{11}$ after HNO_3 treatment. Fig. S4c is the overlapped color image of Figs. S4d-S4h. Fig. S4b is the enlargement of Fig. S4a.

ESI. 4 EDS-based elemental analyses of $ZnRh_2O_4/Ag/Bi_4V_2O_{11}$ photocatalyst (Fig. S5).

EDS-based elemental analysis results for $ZnRh_2O_4/Ag/Bi_4V_2O_{11}$ after HNO_3 treatment are shown in Figs. S5a–S5c (Fig. S5a is the same as Fig. 4a). The large particle in the middle and the small particles around the large particle correspond to $Bi_4V_2O_{11}$ and $ZnRh_2O_4$, respectively, as shown in Fig. S5a. Figure S5b shows the atomic percentages of Ag, Bi, V, Zn, and Rh measured along the line from the area of $ZnRh_2O_4$ (A_1) to that of $Bi_4V_2O_{11}$ (A_2), and Fig. S5c show those along the line from B_1 to B_2. In both cases, the atomic percentages of Zn and Rh decreased at the boundary of $ZnRh_2O_4$ and Ag, and those of Bi and V increased at the boundary of Ag and $Bi_4V_2O_{11}$. Accordingly, the percentage of Ag increased and decreased at the boundaries of $ZnRh_2O_4$ and Ag, and Ag and $Bi_4V_2O_{11}$, respectively. This result indicates that Ag existed at the interface between $ZnRh_2O_4$ and $Bi_4V_2O_{11}$. Note that the Ag particle size ranged from ~200 to 500 nm.

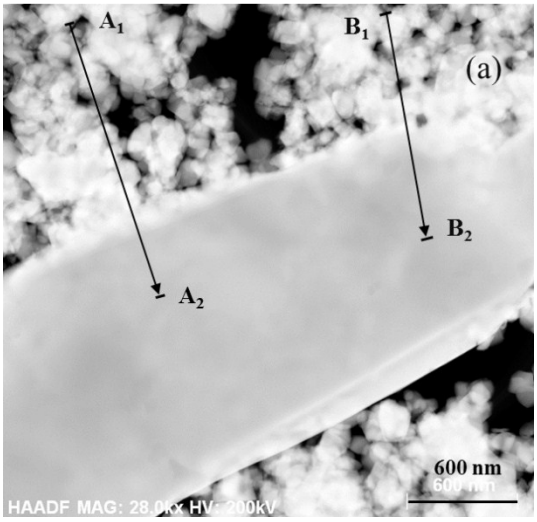

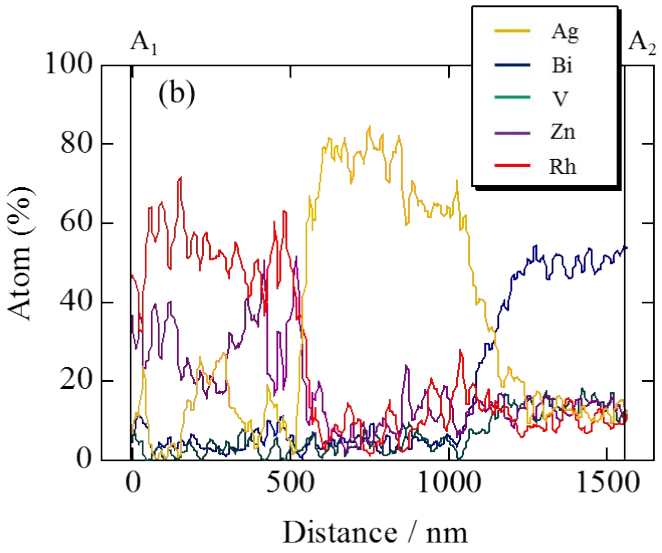

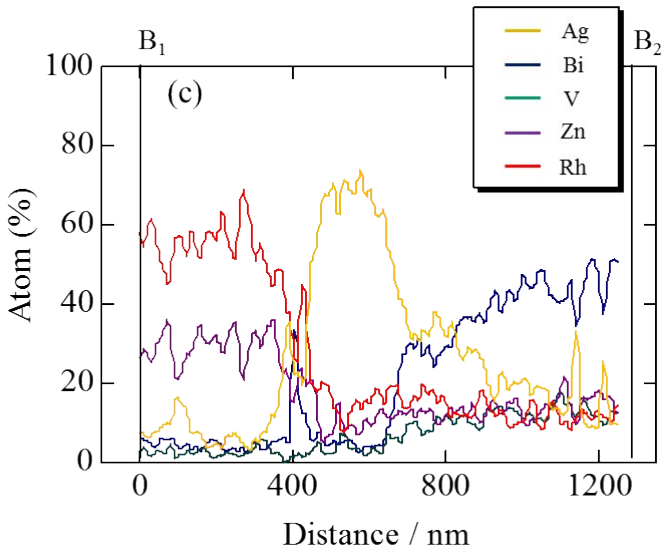

Fig. S5 STEM image of $ZnRh_2O_4/Ag/Bi_4V_2O_{11}$ (a). In (a), the lines along which elemental analyses were performed are shown (A_1 to A_2 and B_1 to B_2). Atomic percentages of Ag, Bi, V, Zn, and Rh measured from the area of $ZnRh_2O_4$ (A_1) to that of $Bi_4V_2O_{11}$ (A_2) (b) and those along the line from B_1 to B_2 (c).

ESI. 5 Complementary water-splitting tests (Fig. S6).

Figure S6 shows the time courses of H_2 and O_2 evolution using only $Bi_4V_2O_{11}$ powder from pure water under irradiation with identical visible light to the case shown in Fig. 7. Neither H_2 nor O_2 was detected. Therefore, $Bi_4V_2O_{11}$ cannot split pure water by itself.

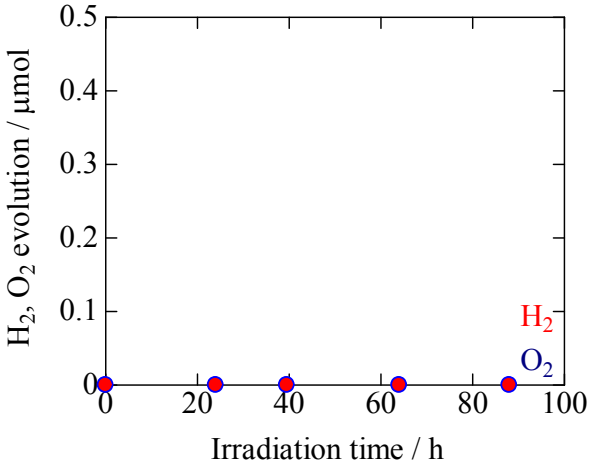

Fig. S6 Time courses of H_2 (red circles) and O_2 (blue circles) evolution from pure water in the presence of $Bi_4V_2O_{11}$ under irradiation with a xenon lamp equipped with a Y-44 filter.

ESI. 6 Complementary tests of half reaction of water (Fig. S7) and water-splitting (Figs. S8, S9).

As will be shown in Scheme S1a, the conduction band bottom potential of $Bi_4V_2O_{11}$ (~0.73 V vs. SHE) is more positive than that of H_2 evolution, thus it is unable to evolve H_2 thermodynamically. To confirm this, O_2 evolution was monitored in the presence of $Bi_4V_2O_{11}$ (60 mg) with the aid of methanol (20 vol%) as a sacrificial agent (from the aqueous methanol solution, 12 mL) irradiated with visible light from the xenon lamp equipped with Y-44 filter (> 420 nm) in Fig. S7. As expected, H_2 was not detected at all, demonstrating that $Bi_4V_2O_{11}$ cannot be the H_2 evolution site in the $ZnRh_2O_4/Ag/Bi_4V_2O_{11}$ system.

Similarly, the valence band top potential of $ZnRh_2O_4$ (~0.056–0.232 V vs. SHE) is more negative than that of O_2 evolution, thus it is unable to evolve O_2 thermodynamically. We have already reported that H_2 was observed in the presence of $ZnRh_2O_4$ with the aid of formaldehyde, but not observed with the aid of methanol (ref. 31). This clearly indicates that $ZnRh_2O_4$ even cannot oxidize methanol. Then, we conclude that $ZnRh_2O_4$ even cannot be the O_2 evolution site in the $ZnRh_2O_4/Ag/Bi_4V_2O_{11}$ system.

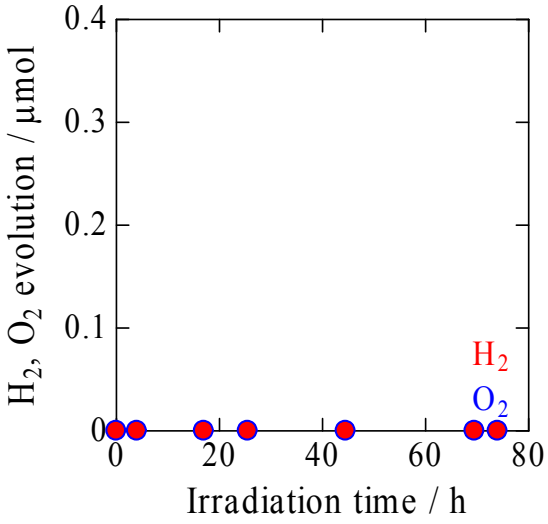

Fig. S7 Time courses of H_2 evolution (red circles) over $Bi_4V_2O_{11}$ photocatalyst irradiated with visible light (> 420 nm) from the aqueous methanol solution as a sacrificial agent. O_2 evolution (blue circles) was also measured, but was not detected at all.

$ZnRh_2O_4$–$Bi_4V_2O_{11}$ hetero-junction photocatalyst ($ZnRh_2O_4/Bi_4V_2O_{11}$) was also prepared using the same procedure, except that Ag_2O powder was excluded from the wet-ball milling process. We examined the pure-water splitting over the $ZnRh_2O_4/Bi_4V_2O_{11}$ photocatalyst irradiated with visible light under the identical conditions in Fig. 6a. As shown in Fig. S8, O_2 was not observed and only a negligible amount of H_2 was observed during the measurement period. In Fig. S8, H_2 and O_2 evolution data from pure water over $ZnRh_2O_4/Ag/Bi_4V_2O_{11}$ irradiated with visible light (>420 nm) were also plotted (the same data marked with solid red and solid blue in Fig. 6a). The results clearly indicated that Ag had an important role in the overall water splitting reaction.

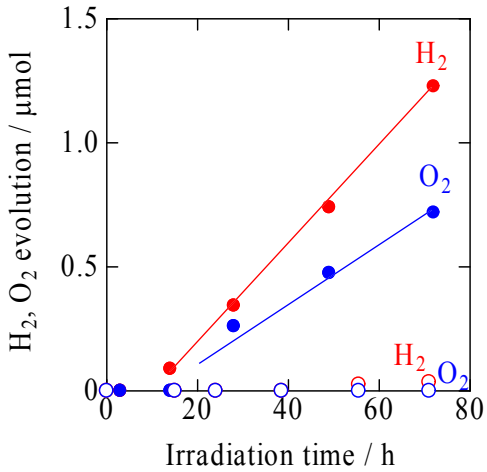

Fig. S8 Time courses of photocatalytic evolution of H_2 (open red) and O_2 (open blue) from pure water over $ZnRh_2O_4/Bi_4V_2O_{11}$ (60 mg) irradiated with visible light (>420 nm). The amounts of H_2 and O_2 from pure water over $ZnRh_2O_4/Ag/Bi_4V_2O_{11}$ are also plotted (closed red and blue, the same as plots in Fig. 6a).

Next we also examined the pure-water splitting by the mixture of $ZnRh_2O_4$, Ag, and $Bi_4V_2O_{11}$ (molar ratio of 6:1:3) irradiated with visible light under the identical conditions in Fig. 6a and Fig. S8. As shown in Fig. S9, neither H_2 nor O_2 was observed at all. In Figs. 6a, S8 and S9, we clearly demonstrated that H_2 and O_2 were evolved only when we prepared the Ag-inserted hetero-junction photocatalyst ($ZnRh_2O_4/Ag/Bi_4V_2O_{11}$) and also Ag had an important role in the overall water splitting reaction.

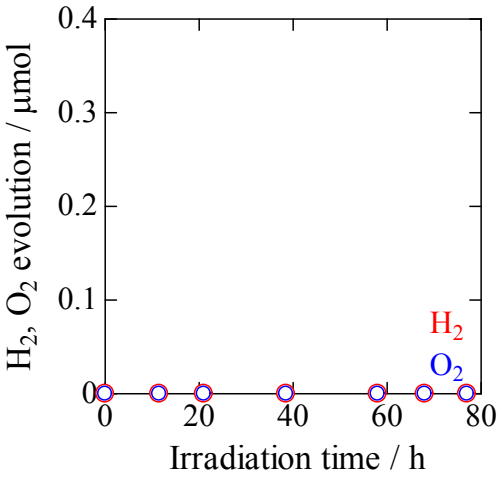

Fig. S9 Time courses of photocatalytic evolution of H_2 (open red) and O_2 (open blue) from pure water over the mixture of $ZnRh_2O_4$, Ag, and $Bi_4V_2O_{11}$ (molar ratio of 6:1:3, 60 mg in total) irradiated with visible light (>420 nm).

ESI. 7 Complementary data related to water-splitting tests using GCMS (Table S1).

We performed quantitative analyses using the GCMS results after 48, 58.5, 72, and 88 h irradiation with the 700 nm LED as shown in Table S1. In the system, we concluded that the unexpectedly detected N_2 originated from external air that entered the GCMS system in our previous report.[23,26] Thus, the $^{16}O^{16}O$ value was calculated ($^{16}O^{16}O$ (calc.)) from the experimental values ($^{16}O^{16}O$ (obs.), $^{14}N^{14}N$ (obs.)), as shown in Table S1, using the equation $^{16}O^{16}O$ (calc.) = $^{16}O^{16}O$ (obs.) – ($^{14}N^{14}N$ (obs.) / 0.78) × 0.21.

Table S1 GCMS results of water splitting by $ZnRh_2O_4$/Ag/$Bi_4V_2O_{11}$ irradiated with 700 nm LED in water containing 33% $H_2{}^{18}O$ for 48, 58.5, 72, and 88 h.

Irradiation time / h	$^{14}N^{14}N$ (obs.) / μmol	$^{16}O^{16}O$ (obs.) / μmol	$^{16}O^{18}O$ (obs.) / μmol	$^{18}O^{18}O$ (obs.) / μmol	$^{16}O^{16}O$ (calc.) / μmol	Total O_2*) / μmol
48	4.30×10^{-1}	1.42×10^{-1}	1.72×10^{-2}	4.33×10^{-3}	2.11×10^{-2}	4.26×10^{-2}
58.5	5.29×10^{-1}	1.84×10^{-1}	2.70×10^{-2}	6.55×10^{-3}	4.13×10^{-2}	7.19×10^{-2}
72	6.00×10^{-1}	2.33×10^{-1}	5.15×10^{-2}	1.34×10^{-2}	7.09×10^{-2}	1.36×10^{-1}
88	6.89×10^{-1}	2.78×10^{-1}	8.98×10^{-2}	2.14×10^{-2}	9.24×10^{-2}	2.04×10^{-1}

*) total O_2 = $^{16}O^{16}O$ (calc.) + $^{16}O^{18}O$ (obs.) + $^{18}O^{18}O$ (obs.)

Note that the ratio of $^{16}O^{16}O$ (calc.):$^{16}O^{18}O$ (obs.):$^{18}O^{18}O$ (obs.) was 4.08:3.97:0.946 after 88 h irradiation.

ESI. 8 The energy band diagram of $ZnRh_2O_4$/Ag/$Bi_4V_2O_{11}$ and charge transfer processes (Schemes S1a, S1b).

The band edge positions of $ZnRh_2O_4$, Ag, and $Bi_4V_2O_{11}$ are described in Scheme 1a. Those of $ZnRh_2O_4$ and Ag were determined in our previous paper.[26] That of $Bi_4V_2O_{11}$ is described in the main text. We measured the Seebeck coefficient (S) of $Bi_4V_2O_{11}$ and obtained a positive value, indicating that it is a p-type semiconductor (not shown here). The band alignments of $ZnRh_2O_4$, Ag, and $Bi_4V_2O_{11}$ before and after connecting Ag and $ZnRh_2O_4$, and Ag and $Bi_4V_2O_{11}$ are shown in Scheme S1b. The charge transfer processes are also included in Scheme S1b.

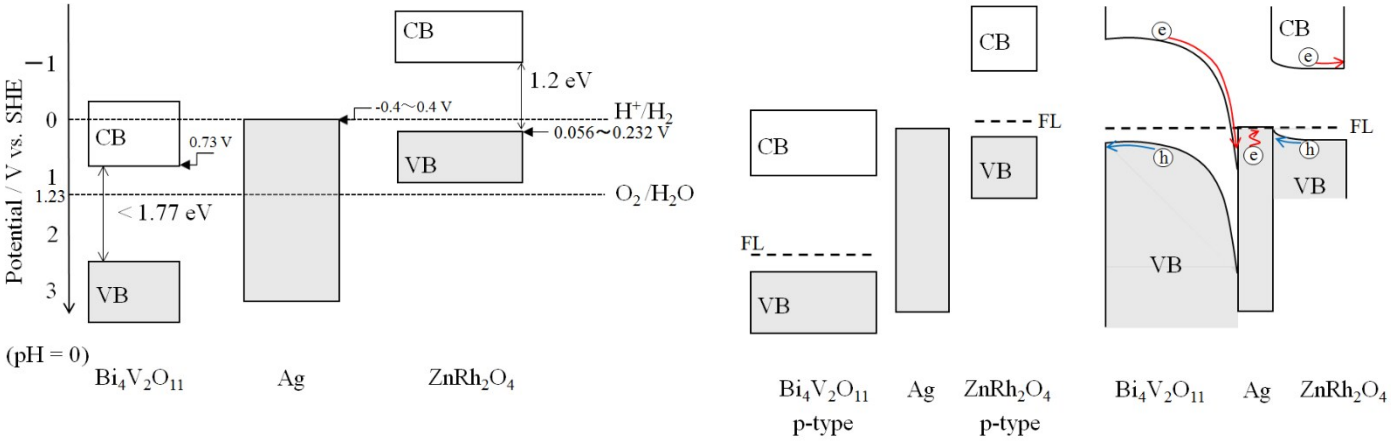

(a) (b)

Scheme S1 Band edge positions of $ZnRh_2O_4$, Ag and $Bi_4V_2O_{11}$ (a) and their band alignments before and after connecting Ag and $ZnRh_2O_4$, and Ag and $Bi_4V_2O_{11}$ (b). The charge transfer processes are also shown in (b).